ARTICLES
https://doi.org/10.1038/s41928-022-00713-1
nature electronics

Check for updates

# Bioinspired in-sensor visual adaptation for accurate perception

Fuyou Liao[1,2], Zheng Zhou[3], Beom Jin Kim[4], Jiewei Chen[1,2], Jingli Wang[1,2,5], Tianqing Wan[2], Yue Zhou[2], Anh Tuan Hoang[4], Cong Wang[1,2], Jinfeng Kang[3], Jong-Hyun Ahn[4] ✉ and Yang Chai[1,2,6] ✉

**Machine vision systems that capture images for visual inspection and identification tasks have to be able to perceive a scene under a range of illumination conditions. To achieve this, current systems use circuitry and algorithms that compromise efficiency and increase complexity. Here we report bioinspired vision sensors that are based on molybdenum disulfide phototransistors and exhibit time-varying activation and inhibition characteristics. Charge trap states are intentionally introduced into the surface of molybdenum disulfide, enabling the dynamic modulation of the photosensitivity of the devices under different lighting conditions. The light-intensity-dependent characteristics of the sensors match Weber's law in which the perceived change in stimuli is proportional to the light stimuli. The approach offers visual adaptation with highly localized and dynamic modulation of photosensitivity under different lighting conditions at the pixel level, creating an effective perception range of up to 199 dB. The phototransistor arrays exhibit image contrast enhancement for both scotopic and photopic adaptation.**

The development of machine vision, which could be of use in applications such as intelligent vehicles and real-time video analysis, requires hardware with high resolution[1], high image-capturing speed[2,3], good stabilization and an ability to detect under a range of lighting conditions[4,5]. Accurate image capture under different light illumination is particularly critical for a correct perception of the environment, as natural light intensity spans a large range of 280 dB (refs. [6–8]). This requires optoelectronic devices that can accurately capture and perceive shadowed and highlighted details. State-of-the-art image sensors using silicon complementary metal–oxide–semiconductor technologies usually have a dynamic range of 70 dB (ref. [9]), which is much narrower than the natural scene. To enable vision under a large illumination intensity range, researchers have explored the use of controlled optical apertures, liquid lenses, adjustable exposure times and de-noising algorithms in post-processing, but these approaches typically require complex hardware and software resources[10–12]. The development of optoelectronic devices that offer visual adaptation functions and a wide perception range at sensory terminals could, however, be used to improve machine vision functionality, reduce hardware complexity and deliver high image recognition efficiency[13–16].

The photoreceptors in human eyes have a limited dynamic range (40 dB) compared with that of a silicon photodetector, but their adaptation characteristics allow us to perceive and recognize various objects under different levels of illumination, from very dark to very bright levels of light. The mechanism of human visual adaptation relies on the localized and dynamic modulation of photosensitivity under different lighting conditions at a pixel level. Two-dimensional layered semiconductors offer strong light–matter interactions, unique defect physics and electrostatic modulation, and can be used to make devices with photosensitivity that can be effectively modulated at a localized level[17–19]. Two-dimensional molybdenum disulfide ($MoS_2$) is particularly promising for use as a channel material in phototransistors[20–22]. Trapped states in $MoS_2$ can affect the optoelectronic response because their density can be comparable to the carrier concentration[23]. Charge trapping and de-trapping processes controlled by a gate terminal in transistor-type devices also allow two contrary photoresponses (excitation and inhibition) to be established under background light illumination in the same device, enabling both photopic and scotopic adaptation[24,25].

In this Article, we report the development of bioinspired vision sensors based on arrays of bottom-gated phototransistors. The transistors use bilayer $MoS_2$ on a high-$\kappa$ dielectric and we intentionally introduce charge trap states at the surface of $MoS_2$. These trap states enable the storage of light information and dynamically modulate the optoelectronic properties of the device at the pixel level. Moreover, the defective states can trap or de-trap electrons of the channel under different gate voltages, which allows us to quantitatively and dynamically modulate the conductance of the device. As a result, the approach offers scotopic and photopic adaptation and can effectively enlarge the perception range of the device in response to different light illumination conditions.

## Scotopic and photopic adaptation

The visual adaptation functions of the human retina rely on various biological cells, including photoreceptors (rods and cones) and horizontal cells (Fig. 1a). Rod cells have high photosensitivity, exclusively responsible for the detection of dim light, whereas cone cells can capture visual information with high light intensity[26]. Both rod and cone cells have a limited detection range for light illumination (40 dB)[6]. Their combination allows to adapt and perceive a wide range from sunlight to starlight (over at least 160 dB)[27]. The working mechanisms for this visual adaptation mainly depend on the switchover between rod and cone cells by negative feedback from horizontal cells and regeneration/bleaching photopigment[28]. The perceived change in stimuli is proportional to the initial stimuli, which is known as Weber's law (Fig. 1b)[29]. Mathematically, it can be described as $\Delta L = k \times L$, where $\Delta L$ is the perceived change,

[1]The Hong Kong Polytechnic University Shenzhen Research Institute, Shenzhen, China. [2]Department of Applied Physics, The Hong Kong Polytechnic University, Hong Kong, China. [3]Institute of Microelectronics, Peking University, Beijing, China. [4]School of Electrical and Electronic Engineering, Yonsei University, Seoul, Republic of Korea. [5]Frontier Institute of Chip and System, Fudan University, Shanghai, China. [6]Research Institute of Intelligent Wearable Systems, The Hong Kong Polytechnic University, Hong Kong, China. ✉e-mail: ahnj@yonsei.ac.kr; ychai@polyu.edu.hk

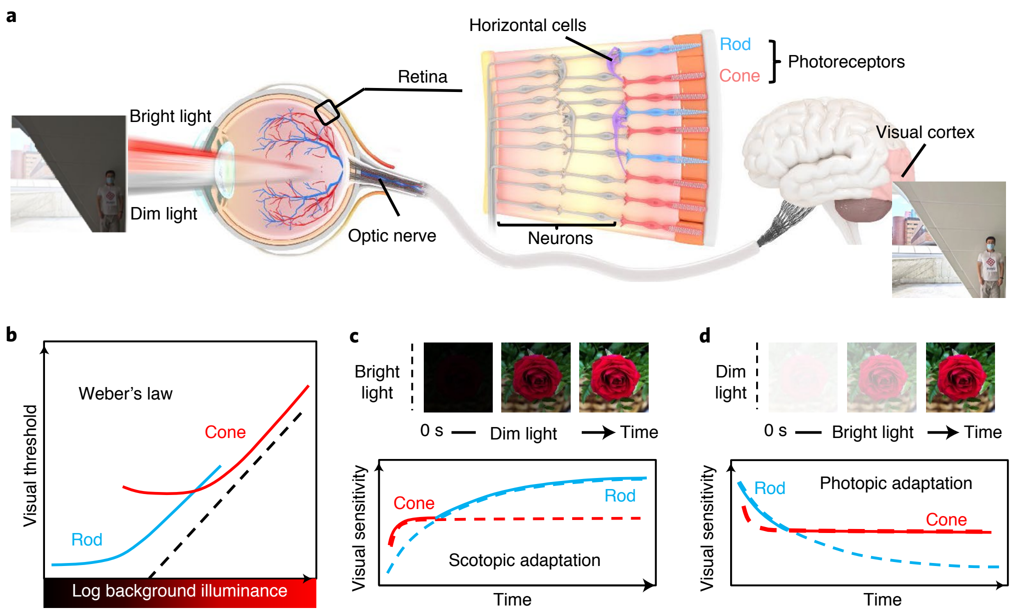


**Fig. 1 | Visual adaptation of the retina. a**, The retina adapts to different illumination intensities through photoreceptors (including cones and rods) and horizontal cells. The objects under extreme light conditions can be well perceived for accurate representation by visual adaptation. **b**, Weber's law: the visual threshold is the minimum amount of energy required for a person to detect a stimulus. The perceived change in stimuli is proportional to the initial light stimuli. **c**,**d**, Scotopic adaptation (**c**) and photopic adaptation (**d**) of the human retina. Top: schematic of the time course of adaptation by images of a flower. Bottom: the mechanism of retina adaptation by the switchover between rod and cone cells. Visual sensitivity is the inverse of visual threshold.

$L$ is the reference stimulus and $k$ is a constant[30]. In other words, as the background illumination increases, the visual threshold of the retina increases accordingly. The retina is less (more) sensitive to a stimulus when the light intensity becomes greater (weaker)[31]. Visual adaptation includes both scotopic and photopic adaptation. When exposed from a bright to a dim ambience, a person can hardly see anything initially and can gradually see the object after visual adaptation (scotopic adaptation), because the retina sensitivity gradually increases over time (Fig. 1c). Photopic adaptation is essentially the reverse of scotopic adaptation. A person is initially dazzled by bright objects and gradually sees them after the adaptation, because the retina sensitivity gradually decreases over time (Fig. 1d).

## Light-intensity-dependent characteristics of the $MoS_2$ phototransistor

A bilayer $MoS_2$ phototransistor with a local bottom-gate configuration (Fig. 2a) allows direct light illumination onto the $MoS_2$ channel region for better optical absorption. Details about the synthesis of $MoS_2$, device fabrication and ultraviolet/ozone (UVO) treatment are described in Methods. Supplementary Fig. 1 shows the Raman spectrum and atomic force microscopy image for identifying the thickness of the $MoS_2$ channel. Supplementary Fig. 2 presents the photoluminescence spectra of bilayer $MoS_2$ with different UVO treatment duration. Spectroscopic and morphological characterizations (Supplementary Fig. 3) verify the uniformity of the as-grown $MoS_2$ on a four-inch Si wafer. Supplementary Fig. 4 exhibits the typical transfer characteristic curves of a $MoS_2$ field-effect transistor under the dark condition, exhibiting n-type transport characteristics. We can observe a clockwise hysteresis loop, which is a result of the charge trapping and de-trapping processes at the surface trap states[32]. The hysteresis voltage window ($\Delta V_{hys}$) is defined as the difference in the gate voltage ($V_G$) at $I_D = 1$ nA, which is estimated to be 2.41 V at an average scan speed of 0.05 V s$^{-1}$. The amount of trap charge density $N_t$ is approximately $2.41\times10^{12}$ cm$^{-2}$ according to $N_t = (\Delta V_{hys} \times C_{ox})/q$, where $C_{ox} = 1.7\times10^{-3}$ F m$^{-2}$ is the oxide capacitance per unit area between the channel and bottom gate ($C_{ox} = \varepsilon_0\varepsilon_{ox}/t_{ox}$; $\varepsilon_{ox} = 7.8$; $t_{ox} = 40$ nm; where $\varepsilon_0$ is vacuum permittivity, $\varepsilon_{ox}$ is the gate insulator permittivity and $t_{ox}$ is the gate insulator thickness) and $q$ is the electron charge[33]. The estimated $N_t$ value is comparable to the carrier density of the $MoS_2$ channel, which can substantially affect the current under different light stimulation conditions[24,33,34]. We fabricated a 10 × 10 $MoS_2$ transistor array on a 2.5 × 3.0 cm$^2$ diced wafer. Supplementary Fig. 5 presents the electrical characterization results of all the devices. Through the optoelectronic characterizations of both pristine and UVO-treated $MoS_2$ phototransistors (Supplementary Figs. 6 and 7), we can observe that the device with the 10 s UVO treatment can introduce a large number of trap states into $MoS_2$ and greatly affect its optoelectronic characteristics.

Figure 2b shows the transfer characteristic curves of the $MoS_2$ phototransistor at $V_D = 1$ V under illumination with different incident power densities ($P_{in}$), ranging from 6 nW cm$^{-2}$ to 60 mW cm$^{-2}$ (660 nm wavelength). The threshold voltage ($V_{TH}$) of the $MoS_2$ phototransistor shifts towards a more negative direction with an increase in $P_{in}$ (Supplementary Fig. 8), which indicates that the carrier density increases under light illumination. In analogy to the visual threshold of the retina, we define a threshold $I_D = 2I_{dark}$ as just a noticeable photocurrent, where $I_{dark}$ represents the drain current at $V_D = 1$ V under dark conditions. Here $I_{dark}$ increases with $V_G$; thus, threshold $I_D$ also increases with $V_G$, which can emulate Weber's law. The effective perception range (PR) of the device can be defined as follows:

$$\mathrm{PR} = 20 \times \log\left[\frac{I_{max}}{I_{min}}\right] (\mathrm{dB}), \quad (1)$$

where $I_{max}$ is $I_D$ at $P_{in} = 60$ mW cm$^{-2}$ and $I_{min}$ is the off current of the device. The calculated effective PR is as high as 199 dB (Supplementary Fig. 9), which is much larger than that in another work[15]. By applying different $V_G$ values, it allows us to modulate the effective PR of a single device. Therefore, we can locally manipulate each pixel in the receptive field to adapt to different illumination conditions and present an accurate representation of an image.

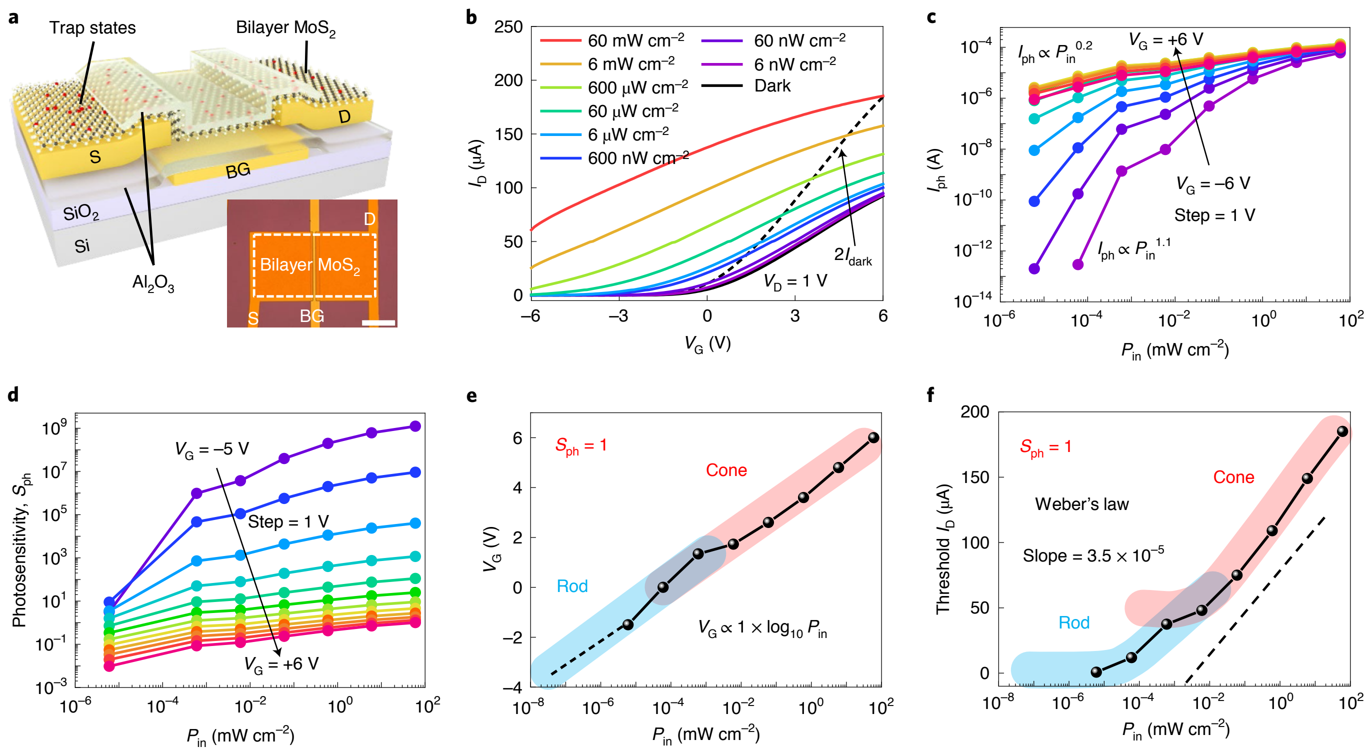


**Fig. 2 | Light-intensity-dependent characteristics of the $MoS_2$ phototransistor. a**, Schematic of the $MoS_2$ phototransistor. Inset: the optical microscopy image of an individual $MoS_2$ phototransistor. The channel width $W$ and channel length $L$ are 200 μm and 10 μm, respectively. Scale bar, 100 μm. S, source; D, drain; BG, bottom gate. **b**, Transfer characteristic curves of the device measured at $V_D = 1$ V under different $P_{in}$ values (660 nm wavelength) at a scan speed of 0.16 V s$^{-1}$. **c**, $I_{ph}$ versus $P_{in}$ for different $V_G$ values. **d**, $S_{ph}$ versus $P_{in}$ for different $V_G$ values. **e**, Relationship between $V_G$ and $P_{in}$ at $S_{ph} = 1$ extracted from **b**. **f**, Threshold $I_D$ as a function of $P_{in}$ at $S_{ph} = 1$ extracted from **b**.

The photocurrent ($I_{ph}$) is defined as $I_{ph} = I_{illumination} - I_{dark}$, where $I_{illumination}$ denotes $I_D$ under the illumination conditions. From the dependence of $I_{ph}$ on $P_{in}$ (Fig. 2c), we observe that $I_{ph}$ increases nearly linearly with $P_{in}$ ($\alpha = 1.1$) at a negative gate bias ($V_G = -6$ V), which suggests that the photogenerated charge carriers are nearly proportional to the incident photon flux. The photoconductive effect is the dominant mechanism in this case[35]. With an increase in gate bias, the relationship between $I_{ph}$ and $P_{in}$ becomes sublinear ($\alpha = 0.2$ at positive $V_G$). This characteristic suggests that the dominant mechanism is the photogating effect associated with the trap states[36,37]. Under light illumination, the localized states can trap the photogenerated holes, which electrostatically induce more electrons, shift the Fermi level and change the channel conductance. Thus, we can control the dominant mechanism responsible for photocurrent generation with $V_G$. In addition, the sublinear photoresponsivity of a $MoS_2$ phototransistor results in a wider photodetection range than a Si photodiode (120 dB)[38,39]. The photosensitivity ($S_{ph}$) is defined as follows[14]:

$$S_{ph} = \frac{I_{ph}}{I_{dark}} = \frac{I_{illumination} - I_{dark}}{I_{dark}}. \quad (2)$$

We extract $S_{ph}$ as a function of $P_{in}$ under different $V_G$ values (Fig. 2d). These characteristics unambiguously show that the $MoS_2$ device has high $S_{ph}$ under negative $V_G$ (similar to the characteristics of rod cells) whereas low $S_{ph}$ under positive $V_G$ (similar to the characteristics of cone cells).

These results verify that $V_G$ is critical to control the photoresponse characteristics ($S_{ph}$) of the $MoS_2$ phototransistor, which enables the emulation of the functions of negative feedback of horizontal cells to switch the photoreception between rod and cone cells in the retina. We can extract the relationship between $V_G$ and $P_{in}$ at $S_{ph} = 1$ (Fig. 2e), which shows a slope of 1 on a semilog scale. According to different $P_{in}$ values, we can apply different $V_G$ values to modulate the characteristics of the $MoS_2$ phototransistor. A positive $V_G$ value tunes the device in the region similar to the cone cells of the photoreceptor, whereas a negative $V_G$ value corresponds to the rod cells of the photoreceptor. We also extract the $P_{in}$-dependent threshold $I_D$ at $S_{ph} = 1$ (Fig. 2f). The threshold $I_D$ increases with an increase in $P_{in}$ at a slope of $3.5 \times 10^{-5}$ on a semilog scale, matching well with the trend of Weber's law ($k = 3.5 \times 10^{-5}$). The $MoS_2$ phototransistor at a positive $V_G$ value (cone) works well for illumination at the photopic level (from $10^{-3}$ to $10^2$ mW cm$^{-2}$), and the device at a negative $V_G$ value (rod) adapts well for illumination at the scotopic level (from $10^{-8}$ to $10^{-3}$ mW cm$^{-2}$ as estimated from the extrapolation of the curve). In this way, the $MoS_2$ phototransistors can fit well with the Weber's law by applying locally different $V_G$ values according to different $P_{in}$ values, which is similar to the switchover between rod and cone cells in photoreceptors by the negative feedback of the horizontal cells of the retina according to different light illumination conditions.

## Time-dependent characteristics of the $MoS_2$ phototransistor

In addition to the switchover between rod and cone cells in photoreceptors, another approach for visual adaptation is the bleaching/regeneration of photopigments. We test the time-dependent $I_D$ of the devices under continuous illumination conditions at fixed $V_G$. We apply negative $V_G$ ($V_G = -2$ V) and record $I_D$ for 120 s under a continuous illumination condition (60 μW cm$^{-2}$), as shown in Fig. 3a. Evidently, $I_D$ gradually increases over time under the continuous illumination condition, which shows a

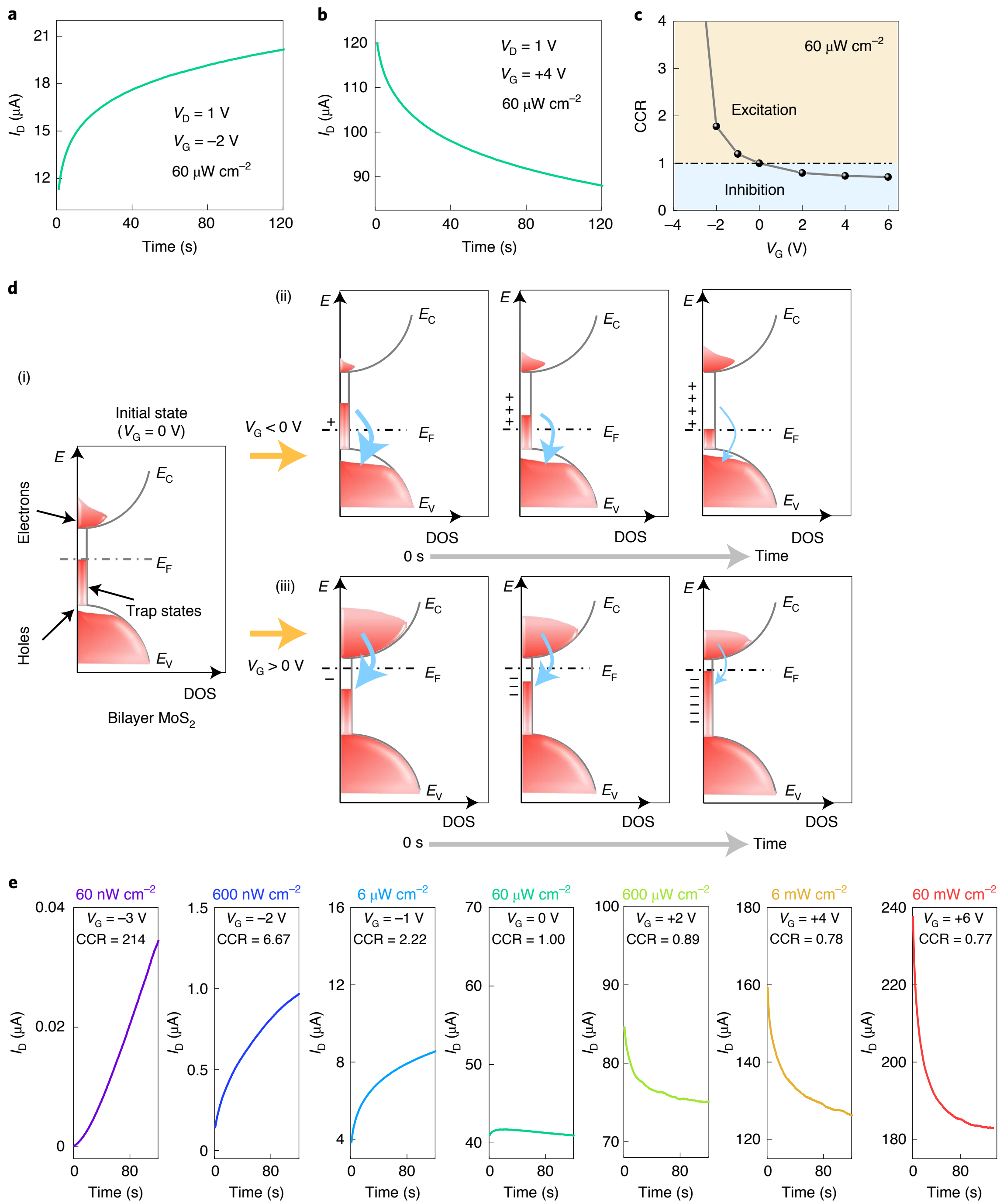


**Fig. 3 | Time-dependent characteristics of the MoS$_2$ phototransistor. a**,**b**, Time-dependent current ($I_D$) of the device under continuous illumination of 60 μW cm$^{-2}$ at $V_G$ values of −2 V (**a**) and +4 V (**b**). **c**, Extracted CCR at different $V_G$ values. **d**, Schematic of the band structure of the MoS$_2$ phototransistor under different gate voltages. DOS, density of states; $E$, electronic energy levels; $E_V$, the valance band. **e**, Time-dependent current ($I_D$) of the device under different $V_G$ values according to different $P_{in}$ values.

current excitation characteristic. We also test the device under the same illumination condition at positive $V_G$ ($V_G$ = +4 V) (Fig. 3b). In contrast to the case at negative $V_G$, $I_D$ gradually decreases over time under the continuous illumination condition, exhibiting a current inhibition behaviour. We also test the time-dependent $I_D$ of the devices under different $V_G$ values ranging from −3 to +6 V under an illumination of 60 μW cm$^{-2}$ and dark conditions (Supplementary Figs. 10 and 11), which shows that the change in $I_D$ over time is dependent on $V_G$. To quantitatively compare the degree of current excitation and inhibition effect, we define the current change ratio (CCR) of the device at different $V_G$ values (Fig. 3c) as follows:

$$\mathrm{CCR} = \frac{I_{\mathrm{D-120s}}}{I_{\mathrm{D-0s}}}, \quad (3)$$

where $I_{\mathrm{D-0s}}$ is the $I_D$ value at the initial state and $I_{\mathrm{D-120s}}$ is the $I_D$ value at 120 s. When $V_G$ is more negative, CCR is larger than 1, indicating a more obvious current excitation effect; when $V_G$ is more positive, CCR is smaller than 1, which suggests a more obvious current inhibition effect.

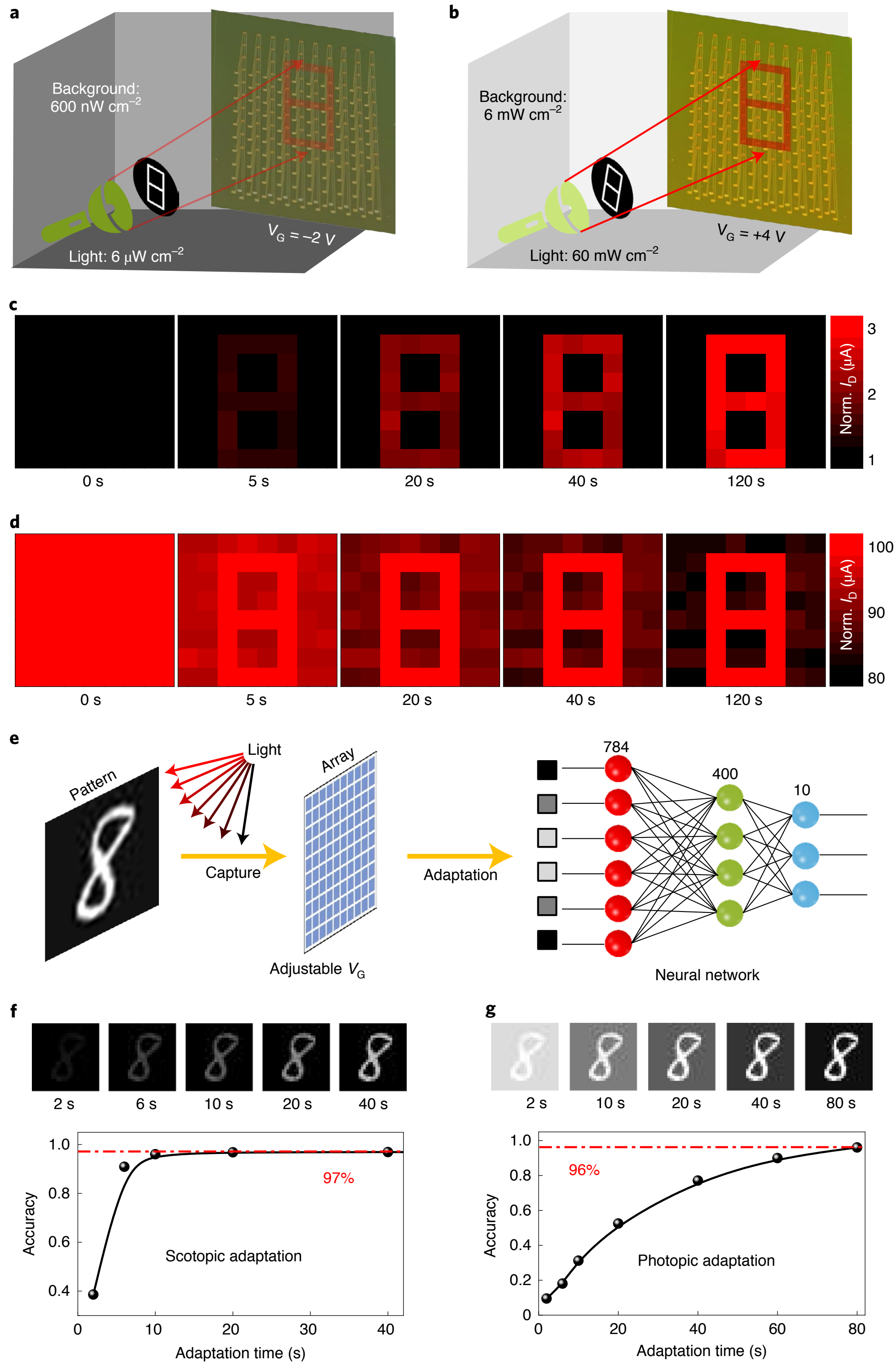


**Fig. 4 | Scotopic and photopic adaptation of $MoS_2$ phototransistor array. a**, Schematic of an 8 × 8 pixel array under a dark background (600 nW cm$^{-2}$) to recognize a low-intensity (6 μW cm$^{-2}$) image for the scotopic adaptation test. **b**, Schematic of an 8 × 8 pixel array under a bright background (6 mW cm$^{-2}$) to recognize a strong-light (60 mW cm$^{-2}$) image for the photopic adaptation test. **c**,**d**, Time courses of scotopic (**c**) and photopic (**d**) adaptation for the pattern of '8'. **e**, Illustration of a machine vision system based on the $MoS_2$ phototransistor array for visual adaptation and an ANN for image recognition. **f**, Top: the simulation result of scotopic adaptation by the MNIST image '8'. Bottom: recognition rate as a function of time for scotopic adaptation. **g**, Top: the simulation result of photopic adaptation by the MNIST image '8'. Bottom: recognition rate as a function of time for photopic adaptation.

To explain the phenomenon of the time-dependent current excitation (inhibition) effect under negative (positive) $V_G$, we illustrate the band diagrams of the $MoS_2$ phototransistor (Fig. 3d). The UVO-treated $MoS_2$ possesses several localized trap states in the bandgap, which mainly result from the defect configurations of S vacancies[40,41]. These trap states are distributed over a broad energy range in the bandgap, exhibiting ambipolar trap states[41]. At the initial state ($V_G = 0$ V), the net charge of these trap states is close to zero (Fig. 3d(i)) (all donor-type traps are occupied with electrons and all acceptor-type traps are vacant). When negative $V_G$ ($V_G = -2$ V) is applied, the Fermi level ($E_F$) is lowered. The donor-type traps above $E_F$ will de-trap electrons and become positively charged after this de-trapping, inducing more electrons in the conductive band ($E_C$) and increasing $I_D$. The shallow donor-type traps first de-trap electrons after negative $V_G$ is applied. As time prolongs, the deeper traps will de-trap electrons (Fig. 3d(ii)). The de-trapping of electrons leads to an increase in $I_D$, which is similar to the regeneration of the photopigment and results in an increase in the visual sensitivity of the photoreceptor. In this case, the fixed negative $V_G$ (horizontal cell) gives rise to electron de-trapping (photopigment regeneration).

In contrast, when a positive $V_G$ ($V_G = +4$ V) is applied, $E_F$ is elevated; further, the acceptor-type states below $E_F$ trap the electrons from $E_C$, which leads to a decrease in electrons in $E_C$ (Fig. 3d(iii)). The shallow acceptor-type traps first trap the electrons after positive $V_G$ is applied. As time prolongs, deep trap states start to trap electrons. The decrease in $I_D$ over time under continuous illumination is analogous to a decrease in the visual sensitivity of photoreceptor cells over time under the bright-light condition. Its mechanism of trapping electrons is similar to the bleaching of the photopigment in the retina, which leads to a decrease in the visual sensitivity of the photoreceptor. Positive $V_G$ (horizontal cell) gives rise to electron trapping (photopigment bleaching).

Based on the time-varying excitation or inhibition characteristics depending on $V_G$, we can realize the visual adaptation function (both scotopic and photopic adaptation) by the $MoS_2$ phototransistor. We can apply more negative $V_G$ under a dim background for excitation characteristics and more positive $V_G$ under a bright light for inhibition behaviour (Fig. 3e). For example, the CCR values are 214.00, 6.67 and 2.22 under a dim light of 60 nW cm$^{-2}$, 600 nW cm$^{-2}$ and 6 μW cm$^{-2}$ by applying $V_G$ of −3, −2 and −1 V (scotopic adaptation), respectively, whereas the CCR values are 0.89, 0.78 and 0.77 under a bright light of 600 μW cm$^{-2}$, 6 mW cm$^{-2}$ and 60 mW cm$^{-2}$ by applying $V_G$ of +2, +4 and +6 V (photopic adaptation), respectively.

In addition, the trapping and de-trapping processes can change the conductance of the $MoS_2$ phototransistor, which can be electrically reset by $V_G$ (Supplementary Fig. 12). Therefore, the $MoS_2$ phototransistor can emulate optoelectronic memory by recording the perceived light information even after turning off the light stimulus due to the persistent photoconductivity effect[23,42]. To demonstrate the image memorization function of the $MoS_2$ phototransistor, we choose a 4 × 4 device array to perceive the pattern of 'A' and record the image after the removal of light illumination (Supplementary Fig. 13).

## Realization of visual adaptation functions by a vision sensor array

Based on the light-intensity-dependent and time-dependent characteristics of the $MoS_2$ phototransistors, we can emulate the sensing and adaptation functions (both scotopic and photopic adaptation) in the human retina with $MoS_2$ phototransistor arrays. We choose an 8 × 8 device array to perceive the pattern of '8'. Supplementary Fig. 14 shows details about the optical microscopy images. For the scotopic adaptation test of the $MoS_2$ phototransistor array, we apply a gate voltage of $V_G = -2$ V to all the devices. The 20 devices corresponding to the image '8' pattern are under a weak light of 6 μW cm$^{-2}$, and the other 44 devices are under a dim background illumination (600 nW cm$^{-2}$) (Fig. 4a). Figure 4c shows the perceived pattern of '8' at a different time under dim light, which was extracted from $I_D$ (Supplementary Figs. 15 and 16 show the detailed test methods and results). To quantitatively evaluate the image quality, we calculate the image contrast ($C$) by the difference in the grey level ($G$) between the two kinds of pixels inside '8' and outside '8' according to the following equation:

$$C = G^*_{\text{illumination}} - G^*_{\text{dark}}, \tag{4}$$

where $G^*_{\text{illumination}}$ is the average $G$ value of the 20 devices under light illumination and $G^*_{\text{dark}}$ is the average $G$ value of the 44 devices under dark. In the biological visual system, the ganglion cell outputs are actually in a fixed range despite the wide range of light intensity, which is very important for the stability of the whole neural system. To keep the perception consistency in the receptive field, we define $I_D = 1$ μA corresponding to the grey level of 0 and $I_D = 3$ μA corresponding to the grey level of 255. The pattern of '8' cannot be recognized at the beginning with zero contrast because of the low photocurrent under a relatively low light illumination. With the visual adaptation effect, its image contrast increases to 51 (5 s), 173 (40 s) and 255 (120 s). The enhancement in image contrast over time is similar to the scotopic adaptation of the retina.

For the photopic adaptation test, all the devices are subjected to $V_G = +4$ V. The 20 devices corresponding to the pattern of '8' are under a strong light of 60 mW cm$^{-2}$ and the other 44 devices are under a bright background illumination (6 mW cm$^{-2}$) (Fig. 4b). We also show the perceived pattern of '8' at a different time under bright light (Fig. 4d), which is extracted from $I_D$ (Supplementary Fig. 17). In this case, we define $I_D = 80$ μA corresponding to the grey level of 0 and $I_D = 100$ μA corresponding to the grey level of 255. The $G$ value of the 20 devices under the illumination of 60 mW cm$^{-2}$ is 255 due to saturation. The image contrast of the pattern of '8' is 0 at 0 s and it increases to 69 (5 s), 164 (40 s) and then 214 (120 s). The 'dazzling' pattern of '8' at the initial stage gradually changes to a comfortable image for the human eye, similar to the photopic adaptation of the retina. $MoS_2$ phototransistors can realize the modulation of image brightness and contrast enhancement when positive $V_G$ is applied.

To quantitatively evaluate the potential of the visual adaptation on enhancing image recognition, we construct a vision system consisting of an adaptive $MoS_2$ phototransistor array and a three-layer artificial neural network (ANN) (Fig. 4e). We use the Modified National Institute of Standards and Technology (MNIST) dataset as the training set to evaluate the image recognition accuracy in a normal environment (the pattern shows the ideal grey level and the image contrast reaches 255). After that, the vision system is exposed to further bright- or dim-light conditions. The $MoS_2$ phototransistor array can capture and perceive patterns through the adaptation process. Detailed information on the machine vision system and simulation is given in Methods and Supplementary Table 1. Figure 4f, top, shows the time course of the MNIST image during scotopic adaptation. The image contrast increases as time increases from 2 to 40 s. The recognition rate (Fig. 4f, bottom) of the visual systems with scotopic adaptation shows obvious improvements from 38.6% at 2 s to 96.9% at 40 s. Fig. 4h, top, shows a photopic adaptation process of an MNIST image. The image contrast is also enhanced as time increases from 2 to 80 s. Figure 4h, bottom, illustrates the recognition rate of visual systems with photopic adaptation, showing obvious improvements in the recognition rate from 9.5% (2 s) to 96.1% (80 s). The adaptation time can be shortened by reducing the perception margin (Supplementary Fig. 18). Supplementary Table 2 shows the comparison among different research works about visual adaptation. These results suggest that this bioinspired in-sensor adaptation strategy can widen the range for image perception under different illumination conditions, which simplify the complexity for hardware and algorithms and enhance the functionalities for processing images at sensory terminals.

## Conclusions

We have reported a vision sensor array that uses bottom-gate bilayer $MoS_2$ phototransistors that can emulate the functions of the horizontal cell and photoreceptor in the retina. Device defect physics, originating from intentionally introduced trap states, enables the dynamic modulation of the device photosensitivity under different lighting conditions. The gate terminal of the phototransistor allows us to control the photoresponse characteristics of the devices according to $P_{in}$ based on the charge trapping and de-trapping mechanisms. Our $MoS_2$ phototransistor arrays exhibit both scotopic and photopic adaptation, offering a broad perception range and image contrast enhancement. This bioinspired in-sensor visual adaptation could be of use in machine vision applications, simplifying or reducing circuitry and complex processing algorithm requirements.

## Methods

**Synthesis of $MoS_2$.** A metal–organic chemical vapour deposition system was utilized to synthesize bilayer $MoS_2$. A four-inch Si wafer with 300-nm-thick oxide was vertically placed in a quartz tube of the furnace after the cleaning process using acetone, isopropanol and deionized water. The furnace was heated to 580 °C and a vacuum of less than $10^{-4}$ torr was maintained. After that, 1.0 s.c.c.m. molybdenum hexacarbonyl (577766, Sigma-Aldrich) and 0.6 s.c.c.m. dimethyl sulfide (471577, Sigma-Aldrich) were introduced as a precursor of Mo and S, respectively. Growth was processed under flows of 310 s.c.c.m. Ar and 5 s.c.c.m. $H_2$ for 23 h to obtain bilayer $MoS_2$, followed by a cooling process up to room temperature in an Ar environment.

**Fabrication of $MoS_2$ phototransistor array.** First, a local bottom-gate electrode (Cr/Au, 3/30 nm) was formed using photolithography, electron-beam evaporation and lift-off process. Second, a 40-nm-thick $Al_2O_3$ dielectric layer was deposited on the bottom gate using atomic layer deposition. Subsequently, the source and drain electrodes (Cr/Au, 3/30 nm) were patterned on $Al_2O_3$ using general photolithography and a lift-off process ($W/L$, 200/10 µm). The bilayer $MoS_2$ film synthesized by metal–organic chemical vapour deposition was transferred onto the substrate and patterned as a channel by reactive-ion etching using $CHF_3/O_2$ plasma[43]. After the removal of the photoresist using a mixture of 100 ml acetone and 5 ml *N*-methyl-2-pyrrolidone, UVO was directly operated on the $MoS_2$ channel with a power intensity of 28 mW cm$^{-2}$ for 10 s to introduce the trap states. Finally, 10-nm-thick $Al_2O_3$ was deposited as an encapsulation layer on the $MoS_2$ channel.

**Characterization of devices.** The electrical measurement of $MoS_2$ devices was conducted in a Lake Shore probe station using a semiconductor analyser (Keithley 4200-SCS). Optoelectronic measurement was performed using a 660 nm laser as the light source; the light passed through an optical fibre to illuminate the devices. An optical power meter (Newport 843-R with an 818-UV/DB optical power detector) was used to calibrate the illumination intensity. All the measurements were conducted in an air atmosphere at room temperature.

**Simulation of ANN.** The $MoS_2$ phototransistor array size is 28 × 28 and the ANN specification is 786 × 400 × 10. In the simulation, the pattern from the MNIST dataset is exposed to different illumination environments and captured by the $MoS_2$ phototransistor array. After the in-sensor adaptation process, the captured pattern in phototransistor array is transformed into one-dimensional data and delivered to the ANN for pattern recognition.

## Data availability

Source data are provided with this paper. The data that support the plots within these paper and other findings of this study are available from the corresponding authors upon reasonable request.

## Code availability

The codes used for simulation and data plotting are available from the corresponding authors upon reasonable request.

Received: 29 June 2021; Accepted: 5 January 2022;
Published online: 3 February 2022

## References


1. Gu, L. et al. A biomimetic eye with a hemispherical perovskite nanowire array retina. *Nature* **581**, 278–282 (2020).
2. Mennel, L. et al. Ultrafast machine vision with 2D material neural network image sensors. *Nature* **579**, 62–66 (2020).
3. Chai, Y. In-sensor computing for machine vision. *Nature* **579**, 32–33 (2020).
4. Zhou, F. & Chai, Y. Near-sensor and in-sensor computing. *Nat. Electron.* **3**, 664–671 (2020).
5. Liao, F., Zhou, F. & Chai, Y. Neuromorphic vision sensors: principle, progress and perspectives. *J. Semicond.* **41**, 013105 (2020).
6. Darmont, A. High dynamic range imaging: sensors and architectures. In *Society of Photo-Optical Instrumentation Engineers* (SPIE, 2013).
7. Wang, C.-Y. et al. Gate-tunable van der Waals heterostructure for reconfigurable neural network vision sensor. *Sci. Adv.* **6**, eaba6173 (2020).
8. Sun, L. et al. In-sensor reservoir computing for language learning via two-dimensional memristors. *Sci. Adv.* **7**, eabg1455 (2021).
9. Ohta, J. *Smart CMOS Image Sensors and Applications* (CRC Press, 2017).
10. Liba, O. et al. Handheld mobile photography in very low light. *ACM Trans. Graph.* **38**, 164 (2019).
11. Rao, Z. et al. Curvy, shape-adaptive imagers based on printed optoelectronic pixels with a kirigami design. *Nat. Electron.* **4**, 513–521 (2021).
12. Kim, M. S. et al. An aquatic-vision-inspired camera based on a monocentric lens and a silicon nanorod photodiode array. *Nat. Electron.* **3**, 546–553 (2020).
13. Xie, D. Xie et al. Photoelectric visual adaptation based on 0D-$CsPbBr_3$-quantum-dots/2D-$MoS_2$ mixed-dimensional heterojunction transistor. *Adv. Funct. Mater.* **31**, 2010655 (2021).
14. Hong, S. et al. Sensory adaptation and neuromorphic phototransistors based on $CsPb(Br_{1-x}I_x)_3$ perovskite and $MoS_2$ hybrid structure. *ACS Nano* **14**, 9796–9806 (2020).
15. Kwon, S. M. et al. Environment-adaptable artificial visual perception behaviors using a light-adjustable optoelectronic neuromorphic device array. *Adv. Mater.* **31**, 1906433 (2019).
16. He, Z. et al. An organic transistor with light intensity-dependent active photoadaptation. *Nat. Electron.* **4**, 522–529 (2021).
17. Wang, Q. H., Kalantar-Zadeh, K., Kis, A., Coleman, J. N. & Strano, M. S. Electronics and optoelectronics of two-dimensional transition metal dichalcogenides. *Nat. Nanotechnol.* **7**, 699–712 (2012).
18. Fiori, G. et al. Electronics based on two-dimensional materials. *Nat. Nanotechnol.* **9**, 768–779 (2014).
19. Liu, Y. et al. Promises and prospects of two-dimensional transistors. *Nature* **591**, 43–53 (2021).
20. Jang, H. et al. An atomically thin optoelectronic machine vision processor. *Adv. Mater.* **32**, e2002431 (2020).
21. Choi, C. et al. Human eye-inspired soft optoelectronic device using high-density $MoS_2$-graphene curved image sensor array. *Nat. Commun.* **8**, 1664 (2017).
22. Choi, C. et al. Curved neuromorphic image sensor array using a $MoS_2$-organic heterostructure inspired by the human visual recognition system. *Nat. Commun.* **11**, 5934 (2020).
23. Lopez-Sanchez, O., Lembke, D., Kayci, M., Radenovic, A. & Kis, A. Ultrasensitive photodetectors based on monolayer $MoS_2$. *Nat. Nanotechnol.* **8**, 497–501 (2013).
24. Nur, R. et al. High responsivity in $MoS_2$ phototransistors based on charge trapping $HfO_2$ dielectrics. *Commun. Mater.* **1**, 103 (2020).
25. Lee, J. et al. Monolayer optical memory cells based on artificial trap-mediated charge storage and release. *Nat. Commun.* **8**, 14734 (2017).
26. Miller, R. E. & Tredici, T. J. *Night Vision Manual for the Flight Surgeon*. (ARMSTRONG LAB BROOKS AFB TX, 1992).
27. Seetzen, H. et al. High dynamic range display systems. In *ACM SIGGRAPH 2004 Papers* 760–768 (Association for Computing Machinery, 2004).
28. Kalloniatis, M. & Luu, C. Light and dark adaptation. In *Webvision: The Organization of the Retina and Visual System* (eds Kolb, H. et al.) (Univ. Utah Health Sciences Center, 1995).
29. Fechner, G. *Elements of Psychophysics* Vol. I (Holt, Rinehart and Winston, 1966).
30. Kandel, E. R. et al. *Principles of Neural Science* Vol. 4 (McGraw-Hill, 2000).
31. Meister, M. & Tessier-Lavigne, M. Low-level visual processing: the retina. *Prin. Neural Sci.* **5**, 577–601 (2013).
32. Jiang, J. et al. Rational design of $Al_2O_3$/2D perovskite heterostructure dielectric for high performance $MoS_2$ phototransistors. *Nat. Commun.* **11**, 4266 (2020).
33. Park, Y., Baac, H. W., Heo, J. & Yoo, G. Thermally activated trap charges responsible for hysteresis in multilayer $MoS_2$ field-effect transistors. *Appl. Phys. Lett.* **108**, 083102 (2016).
34. Kaushik, N. et al. Reversible hysteresis inversion in $MoS_2$ field effect transistorsr. *npj 2D Mater. Appl.* **1**, 34 (2017).
35. Fang, H. & Hu, W. Photogating in low dimensional photodetectors. *Adv. Sci.* **4**, 1700323 (2017).
36. Wu, J. Y. et al. Broadband $MoS_2$ field-effect phototransistors: ultrasensitive visible-light photoresponse and negative infrared photoresponse. *Adv. Mater.* **30**, 1705880 (2018).
37. Kufer, D. & Konstantatos, G. Highly sensitive, encapsulated $MoS_2$ photodetector with gate controllable gain and speed. *Nano Lett.* **15**, 7307–7313 (2015).
38. Pierre, A., Gaikwad, A. & Arias, A. C. Charge-integrating organic heterojunction phototransistors for wide-dynamic-range image sensors. *Nat. Photon.* **11**, 193–199 (2017).
39. Gong, X. et al. High-detectivity polymer photodetectors with spectral response from 300 nm to 1450 nm. *Science* **325**, 1665–1667 (2009).

40. Peng, B. et al. Achieving ultrafast hole transfer at the monolayer $MoS_2$ and $CH_3NH_3PbI_3$ perovskite interface by defect engineering. *ACS Nano* **10**, 6383–6391 (2016).
41. Chen, M. et al. Multibit data storage states formed in plasma-treated $MoS_2$ transistors. *ACS Nano* **8**, 4023–4032 (2014).
42. Zhou, F. et al. Optoelectronic resistive random access memory for neuromorphic vision sensors. *Nat. Nanotechnol.* **14**, 776–782 (2019).
43. Choi, M. et al. Full-color active-matrix organic light-emitting diode display on human skin based on a large-area $MoS_2$ backplane. *Sci. Adv.* **6**, eabb5898 (2020).

## Acknowledgements

This work was supported by China Postdoctoral Science Foundation (2021M692221); Research Grant Council of Hong Kong (15205619); Science, Technology and Innovation Commission of Shenzhen (JCYJ20180507183424383 and SGDX2020110309540000); and the Hong Kong Polytechnic University (1-ZE1T and 1-ZVGH). J.-H.A. acknowledges support from the National Research Foundation of Korea (NRF-2015R1A3A2066337).

## Author contributions

Y.C. conceived the concept and supervised the project. F.L. designed the test protocol and performed the experiments. B.J.K., A.T.H. and J.-H.A. fabricated the devices. F.L., J.C. and J.W. analysed the experimental data. Z.Z., C.W. and J.K. performed the simulations. F.L., Z.Z., T.W., Y.Z. and Y.C. co-wrote the paper. All the authors discussed the results and commented on the manuscript.

## Competing interests

The authors declare no competing interests.

## Additional information

**Supplementary information** The online version contains supplementary material available at https://doi.org/10.1038/s41928-022-00713-1.

**Correspondence and requests for materials** should be addressed to Jong-Hyun Ahn or Yang Chai.

**Peer review information** *Nature Electronics* thanks Sunkook Kim, Tse Nga Ng and the other, anonymous, reviewer(s) for their contribution to the peer review of this work.

**Reprints and permissions information** is available at www.nature.com/reprints.

**Publisher's note** Springer Nature remains neutral with regard to jurisdictional claims in published maps and institutional affiliations.